



# Electrochemical study on nickel aluminum layered double hydroxides as high-performance electrode material for lithium-ion batteries based on sodium alginate binder

Xinyue Li<sup>1</sup> · Marco Fortunato<sup>2</sup> · Anna Maria Cardinale<sup>2</sup> · Angelina Sarapulova<sup>1</sup> · Christian Njel<sup>1</sup> · Sonia Dsoke<sup>1,3</sup>

Received: 12 March 2021 / Revised: 22 June 2021 / Accepted: 13 July 2021 / Published online: 21 July 2021  
© The Author(s) 2021

## Abstract

Nickel aluminum layered double hydroxide (NiAl LDH) with nitrate in its interlayer is investigated as a negative electrode material for lithium-ion batteries (LIBs). The effect of the potential range (i.e., 0.01–3.0 V and 0.4–3.0 V vs. Li<sup>+</sup>/Li) and of the binder on the performance of the material is investigated in 1 M LiPF<sub>6</sub> in EC/DMC vs. Li. The NiAl LDH electrode based on sodium alginate (SA) binder shows a high initial discharge specific capacity of 2586 mAh g<sup>-1</sup> at 0.05 A g<sup>-1</sup> and good stability in the potential range of 0.01–3.0 V vs. Li<sup>+</sup>/Li, which is better than what obtained with a polyvinylidene difluoride (PVDF)-based electrode. The NiAl LDH electrode with SA binder shows, after 400 cycles at 0.5 A g<sup>-1</sup>, a cycling retention of 42.2% with a capacity of 697 mAh g<sup>-1</sup> and at a high current density of 1.0 A g<sup>-1</sup> shows a retention of 27.6% with a capacity of 388 mAh g<sup>-1</sup> over 1400 cycles. In the same conditions, the PVDF-based electrode retains only 15.6% with a capacity of 182 mAh g<sup>-1</sup> and 8.5% with a capacity of 121 mAh g<sup>-1</sup>, respectively. Ex situ X-ray photoelectron spectroscopy (XPS) and ex situ X-ray absorption spectroscopy (XAS) reveal a conversion reaction mechanism during Li<sup>+</sup> insertion into the NiAl LDH material. X-ray diffraction (XRD) and XPS have been combined with the electrochemical study to understand the effect of different cutoff potentials on the Li-ion storage mechanism.

**Keywords** Layered double hydroxide · Lithium-ion batteries · Sodium alginate · Electrode materials · Conversion reaction

## Introduction

Rechargeable lithium-ion batteries (LIBs) dominate the market for several decades due to their outstanding energy density, high working voltage, and long cycle life [1–4]. Graphitic carbon has long been employed as the most common

intercalation-type negative electrode material. However, graphite is limited by its relatively low theoretical capacity (372 mAh g<sup>-1</sup>) [5]. The necessity of increasing the energy and power density has made it urgent to discover new types of anode materials with higher capacity than graphite, good rate performance, and cycling stability.

Layered metal hydroxides, like Ni(OH)<sub>2</sub>, have been considered as negative electrode materials for LIBs owing to their structure with large interlayer spacing that enables rapid transfer of lithium ions [6, 7]. Li et al. reported promising performance of β-Ni(OH)<sub>2</sub>-reduced graphene oxide composites as an anode for LIBs [8]. Nevertheless, the sluggish rate capability and poor cycling stability of Ni(OH)<sub>2</sub> have hindered its application [9]. Compared with single metal hydroxides, layered double hydroxides (LDHs), as a class of two-dimensional anionic clays [10], show larger basal spacing owing to the pillaring of interlayer species, which can favor the intercalation of Li<sup>+</sup>. LDHs, which can be expressed as [M<sup>2+</sup><sub>1-x</sub>M<sup>3+</sup><sub>x</sub>(OH)<sub>2</sub>]<sup>x+</sup>(A<sup>n-</sup>)<sub>x/n</sub>·mH<sub>2</sub>O, offer various possible valence states provided by mixed metal ions (M<sup>2+</sup> and

---

This work is dedicated to the memory of Roberto Marassi, a brilliant mentor who instilled in his students the passion for electrochemistry and still inspiring the next generation of scientists.

---

✉ Sonia Dsoke  
sonia.dsoke@kit.edu

<sup>1</sup> Institute for Applied Materials (IAM), Karlsruhe Institute of Technology (KIT), Hermann-von-Helmholtz-Platz 1, Eggenstein-Leopoldshafen 76344, Germany

<sup>2</sup> Dipartimento Di Chimica E Chimica Industriale, Università Di Genova, Via Dodecaneso 31, Genova 16146, Italy

<sup>3</sup> Helmholtz-Institute Ulm for Electrochemical Energy Storage (HIU), P.O. Box 3640, Karlsruhe 76021, Germany

$M^{3+}$ ) in the host layer. Based on their lamellar structure that consists of positive charged brucite-like host layers and exchangeable charge-balancing interlayer anions (i.e.,  $A^{n-}$  such as  $\text{NO}_3^-$ ,  $\text{CO}_3^{2-}$ ,  $\text{Cl}^-$ ,  $\text{SO}_4^{2-}$ ) [11], LDHs possess adjustability of physical and chemical properties, which can be achieved by replacing the metal cations, tuning the molar ratio of metals, and altering the interlayer anions. Therefore, this type of layered materials find applications in many fields, including catalysis [12–14], biochemistry [15, 16], wastewater remediation, and supercapacitors [17–22].

In the field of rechargeable batteries, LDHs are typically employed as precursors or templates for the synthesis of metal oxides, which are then used as electrode's active materials in LIBs. In fact, the application of LDH-based composites as electrode materials was reported only very recently. For instance, Shi et al. [23] presented the fabrication of CoNi LDH and graphene-wrapped CoNi LDH as negative electrodes for LIBs. The graphene-wrapped CoNi LDH composite electrode exhibits a higher reversible specific capacity of  $1428.0 \text{ mAh g}^{-1}$  at  $0.05 \text{ A g}^{-1}$  and excellent capacity retention of 75% after 10,000 cycles at  $10 \text{ A g}^{-1}$  in the potential range of 0.01–3.0 V vs.  $\text{Li}^+/\text{Li}$  compared with the CoNi LDH electrode. Zhang et al. [24] synthesized a  $\text{Co}_3\text{V}_2\text{O}_8@/\text{NiCo}$  LDH material, which reveals a reversible specific capacity of  $1329.4 \text{ mAh g}^{-1}$  at  $1 \text{ A g}^{-1}$  after 500 cycles and good cycling performance ( $893.1 \text{ mAh g}^{-1}$  at  $5 \text{ A g}^{-1}$  after 950 cycles). This bi-material shows improved performance compared to the pure  $\text{Co}_3\text{V}_2\text{O}_8$  and to the pure NiCo LDHs in the potential range 0.01–3.0 V vs.  $\text{Li}^+/\text{Li}$ . On the other hand, with the increasing need to cut the cobalt consumption that is raising sustainability and environmental concerns [25–27], it is crucial to explore and develop cobalt-free LDHs. With this aim, a NiFe-LDHs/reduced graphene oxide composite anode material has been synthesized by Zhang et al. [28]. This material shows an initial capacity of  $602.8 \text{ mAh g}^{-1}$  after 80 cycles at  $500 \text{ mA g}^{-1}$  in the potential range 0.01–3.0 V vs.  $\text{Li}^+/\text{Li}$ . Although LDHs have been reported as novel electrode materials for lithium-ion batteries, research dedicated to understanding the Li-storage mechanism, which is fundamental for optimizing the performance, is limited. Besides, the role of the binder, which is a critical component in influencing the cycling ability and rate performance, is rarely investigated for this kind of compound [29].

In this work, we report, for the first time, the direct application of NiAl LDH with nitrates as its interlayer anion as a negative electrode material for LIBs. The NiAl LDH electrode delivers high specific capacity and shows excellent cycling stability with sodium alginate (SA) as the binder. Ex situ XAS analysis reveals that the NiAl LDH stores Li ions via a conversion-type mechanism during the discharge–charge processes.

## Experimental section

### Preparation of NiAl LDH

NiAl LDH was obtained by a facile and straightforward one-pot hydrothermal reaction. All reagents (aluminum nitrate nonahydrate ( $\text{Al}(\text{NO}_3)_3 \cdot 9\text{H}_2\text{O}$ ), nickel nitrate hexahydrate ( $\text{Ni}(\text{NO}_3)_2 \cdot 6\text{H}_2\text{O}$ ), and urea ( $\text{CO}(\text{NH}_2)_2$ ) provided by Sigma-Aldrich) were of analytical purity and were directly used without further purification. By following the procedure in [30], a solution has been prepared by dissolving 30 mmol of  $\text{Ni}(\text{NO}_3)_2 \cdot 6\text{H}_2\text{O}$ , 45 mmol of urea, and 15 mmol of  $\text{Al}(\text{NO}_3)_3 \cdot 9\text{H}_2\text{O}$  (a Ni:Al ratio of 2:1) in 150 mL of deionized water. This solution was then transferred into a Teflon-lined stainless steel autoclave of 200-mL capacity at a temperature of  $100^\circ\text{C}$ . After a 24 h of hydrothermal process, the product was filtered and washed with water and ethanol several times. The NiAl LDH was finally obtained by drying the product in an oven for one night at  $70^\circ\text{C}$ .

### Structural and physical characterization

The X-ray diffraction (XRD) patterns were collected using STOE STADI P X-ray powder diffractometers equipped with Mythen1K detectors with  $\text{Mo K}\alpha 1$  radiation ( $\lambda = 0.70932 \text{ \AA}$ ). The diffraction pattern was analyzed by full-profile Rietveld refinements, using the software package WinPLOTR [31]. The instrument used for the field emission scanning electron microscope (FE-SEM) characterization was a ZEISS SUPRA 40 VP. FT-IR spectroscopy was performed using a Spectrum 65 FT-IR Spectrometer (PerkinElmer, Waltham, MA, USA) equipped with a KBr beam splitter and a DTGS detector by using an ATR accessory with a diamond crystal; the spectra were recorded from 4000 to  $600 \text{ cm}^{-1}$ . The X-ray photoelectron spectroscopy (XPS) was acquired using a Thermo Scientific K-alpha spectrometer. The samples were analyzed using a micro-focused, monochromated Al  $\text{K}\alpha$  X-ray source ( $1486.6 \text{ eV}$ ,  $400\text{-}\mu\text{m}$  spot size). XPS spectra were recorded with a concentric hemispherical analyzer at the pass energy of  $50 \text{ eV}$  and fit with one or more Voigt profiles (binding energy uncertainty:  $\pm 0.2 \text{ eV}$ ). Scofield sensitivity factors were applied for quantification [32] using the Advantage software package. On the electrode samples, all spectra were referenced to the  $\text{CF}_2$  component originated from the polyvinylidene fluoride (PVDF) binder centered at  $290.7 \text{ eV}$  binding energy. Regarding the NiAl LDH-SA sample, the spectral calibration was done on the C 1 s peak (C–C, C–H) at  $285.0 \text{ eV}$  binding energy controlled by means of the photoelectron peaks of metallic

Cu, Ag, and Au, respectively. X-ray absorption near-edge structure (XANES) and extended X-ray absorption fine structure (EXAFS) spectra for the Ni K-edge of the samples with the different state of charge were conducted on the P65 beamline, PETRA III, German Electron Synchrotron in Hamburg (DESY). XAS spectra were collected at Ni K-edge in transmission geometry with the continuous scan mode. The double-crystal fixed-exit monochromator was equipped with Si (111) crystals. Ex situ samples for XAS measurements were obtained by applying a constant potential to equilibrate the system after the desired potential is reached. The specific surface area of sample was determined by the Brunauer–Emmett–Teller (BET) method. The sample is heated for 4 h at 100 °C in a 500- $\mu\text{mHg}$  vacuum to remove contamination on the surface. A known volume of gas is added to the sample chamber and the pressure is recorded at 77.4 K. The sample was analyzed with a multipoint measurement with a micromeritics ASAP 2020 Plus Physisorption apparatus.

### Electrodes preparation and electrochemical tests

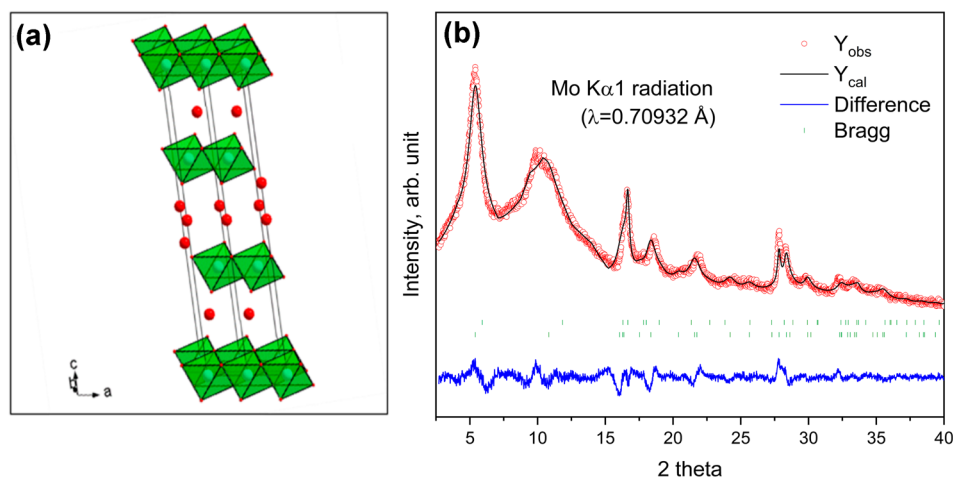
NiAl LDH electrodes have been prepared as follows: 70 wt% of the as-prepared NiAl LDH was mixed by stirring in a quartz mortar for 10 min with 20 wt% conductive carbon black (TIMCAL® Super C65) and 10 wt% of binder in the appropriate solvent. For comparison, polyvinylidene fluoride (PVDF, R6020/1001, Solvay) and sodium alginate (SA, Sigma-Aldrich) were chosen as the binders. The solvents used to dissolve PVDF and SA were N-methyl-2-pyrrolidone (NMP, GC 99.5%, Merck KGaA) and 9:1 water/isopropanol, respectively. The blended slurries were then coated on a 10- $\mu\text{m}$ -thick copper foil current collector with a wet thickness of  $\sim 110 \mu\text{m}$ , followed by drying in an oven at 80 °C for 12 h. After that, the coated electrodes were cut into individual disks of 12-mm diameter ( $\sim 11\text{-}\mu\text{m}$  thickness) with  $\sim 0.7\text{-mg}$  mass loading of NiAl LDH. The

electrodes with different binders are denoted as NiAl LDH-SA and NiAl LDH-PVDF, respectively. CR2032 coin cells were built in an argon-filled glovebox (MB200, MBraun GmbH) consisting of the as-prepared working electrode, a lithium foil counter electrode (15-mm diameter, Alfa Aesar), a glass fiber separator (Whatman glass microfiber filter, 675- $\mu\text{m}$  thickness), and LP30 electrolyte (1 M  $\text{LiPF}_6$  in ethylene carbonate/dimethyl carbonate in a weight ratio of 1:1, BASF). The electrochemical tests (galvanostatic charge–discharge (GCD) and cyclic voltammetry (CV)) were carried out on a multichannel potentiostat (VMP3, Bio-Logic). The electrochemical cells were kept in a binder climate chamber at 25 °C during the electrochemical experiments. Two potential ranges (0.01–3.0 V and 0.4–3.0 V vs.  $\text{Li/Li}^+$ ) were employed for GCD and CV tests.

### Results and discussion

The as-prepared NiAl LDH was characterized by XRD (Fig. 1) and the crystal structure was determined by Rietveld refinement with the assistance of the FullProf software package. The XRD reflections of NiAl LDH can be indexed using a structure model of oxonium nickel oxide (ICSD 24,986). The broad reflections can be explained by phase separation with the same rhombohedral R-3 m space group, suggesting the different d-spacing between 6 and 8 Å. The FT-IR spectrum is shown in Fig. S1. The broad absorption band at  $3410 \text{ cm}^{-1}$  can be attributed to the O–H stretching vibrations of the hydroxyl groups and the presence of water molecules in the interlayer of LDH [22]. Specifically, the interlayered lattice water is hydrogen bonded to the transition metal slabs [33, 34]. It is expected that during delithiation, the crystal water molecules remain in the interlayer space [35, 36]. The weak peak at  $1632 \text{ cm}^{-1}$  is ascribed to the vibrations of the in-plane bending mode of water molecules. The sharp characteristic absorption band at  $1348 \text{ cm}^{-1}$  corresponds to

**Fig. 1** **a** Crystal structure of NiAl LDH and **b** Rietveld refinement of X-ray powder diffraction data of NiAl LDH polycrystalline material



the stretching vibration mode of  $\text{NO}_3^-$ , which confirms the absorption of  $\text{NO}_3^-$  in the interlayer of NiAl LDH materials. The bands at  $749$  and  $652\text{ cm}^{-1}$  are due to the stretching and bending modes of Al–OH and Ni–OH, respectively. XRD and FT IR spectra demonstrate the successful synthesis of NiAl LDH with  $\text{NO}_3^-$  in the interlayer. Based on the thermogravimetric curve (Fig. S2) and the feeding molar ratio of  $\text{Ni}(\text{NO}_3)_2 \cdot 6\text{H}_2\text{O}$  and  $\text{Al}(\text{NO}_3)_3 \cdot 9\text{H}_2\text{O}$  (a Ni:Al ratio of 2:1), the molecular formula of the as-prepared NiAl LDH is expected to be  $[\text{Ni}_{1-x}\text{Al}_x(\text{OH})_2]^{x+}(\text{NO}_3^-)_x \cdot m\text{H}_2\text{O}$  with  $m = 0.16$  and  $x \approx 0.33$ .

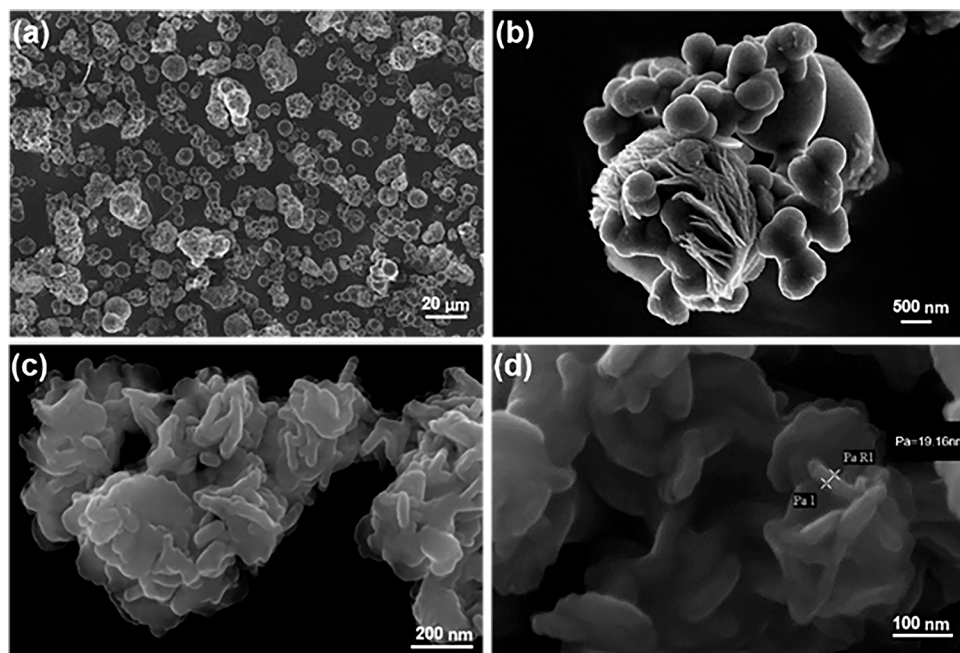
The morphology of NiAl LDH was characterized via FE-SEM, which is shown in Fig. 2. The homogeneously dispersed cluster of lamellae with  $10\text{--}30\ \mu\text{m}$  of diameter can be observed on the image at low magnification (Fig. 2a). The higher magnification image (Fig. 2c) shows that the NiAl LDH lamellae cluster has a flower-like structure arranged in a concentric form and it is highly nano crystallized. Besides, a thickness of the NiAl LDH lamellae ranging from  $20$  to  $40\text{ nm}$  can be observed in Fig. 2d. Furthermore,  $\text{N}_2$  isotherms of NiAl LDH have been performed to determine the surface area and pore size. The BET-specific surface area of NiAl LDH is  $46.85\text{ m}^2\text{ g}^{-1}$ , and the average pore diameter is around  $8.54\text{ nm}$  (Fig. S3).

The surface electronic state of NiAl LDH materials is illustrated by XPS, as shown in Fig. 3. Survey XPS spectrum reveals the presence of Nickel (Ni 2p, Ni 3p, or Ni 3 s), aluminum (Al 2 s or Al 2p), oxygen (O 1 s), nitrogen (N 1 s), and carbon (C 1 s). High-resolution XPS spectra of Ni 2p<sub>3/2</sub>, Al 2 s, O 1 s, N 1 s, and C 1 s are shown in Fig. 3b–f. The peak of Ni 2p<sub>3/2</sub> located at  $856.3\text{ eV}$  with its shake-up satellites, as

shown in Fig. 3b, is a signature of various Ni (+II) species in NiAl LDHs [37, 38]. The Al 2 s–Ni 3 s spectrum shows two peaks centered at  $114.1\text{ eV}$  and  $119.7\text{ eV}$  (Fig. 3c), which are signatures of Ni and Al chemical environments. The peak positions of these atoms are the signature of  $\text{Ni}^{2+}$  and  $\text{Al}^{3+}$  environments in the crystal structure of NiAl LDH material [39]. The O 1 s spectrum (Fig. 3d) shows signals coming from all oxygenated species at the surface. The prominent oxygen peak at  $532\text{ eV}$  corresponds to a mix of oxygen from NiAl LDH structure and other oxygenated species from surface contamination environments (CO and COO groups) [40]. The XPS analysis demonstrates that the  $\text{Ni}^{2+}$  and  $\text{Al}^{3+}$  elements coexist in the product, which is in good accordance with the prediction. Concerning the C 1 s spectrum, three peaks are presented. The main peak on C 1 s spectrum at  $285\text{ eV}$  corresponds to hydrocarbon contamination ( $285\text{ eV}$ ). The peaks centered at  $286.5\text{ eV}$  and  $288.5\text{ eV}$  correspond, respectively, to mono- and bi-oxygenated carbon environments. Carbon species come from surface contamination of NiAl with the air environment. N 1 s spectra display one peak at  $407.1\text{ eV}$ , corresponding to nitrates ( $\text{NO}_3^-$ ) present in the interlayer of NiAl LDHs material. The XPS analysis of the prepared NiAl LDH material determines the atoms' chemical environments present in the crystalline structure and it agrees with the FT-IR and XRD measurements made on the material.

The NiAl LDH composite electrodes based on the two binders (SA and PVDF) have been characterized via CV and GCD. Figure 4a displays the CV curves of NiAl LDH-SA electrode at  $0.1\text{ mV s}^{-1}$  in the potential window of  $0.01\text{--}3.0\text{ V}$  (vs. Li/Li<sup>+</sup>). In the first cycle, the weak and

**Fig. 2** FE-SEM micrographs of NiAl LDH. **a** overview; **b** low magnification image; **c** & **d** high-magnification images





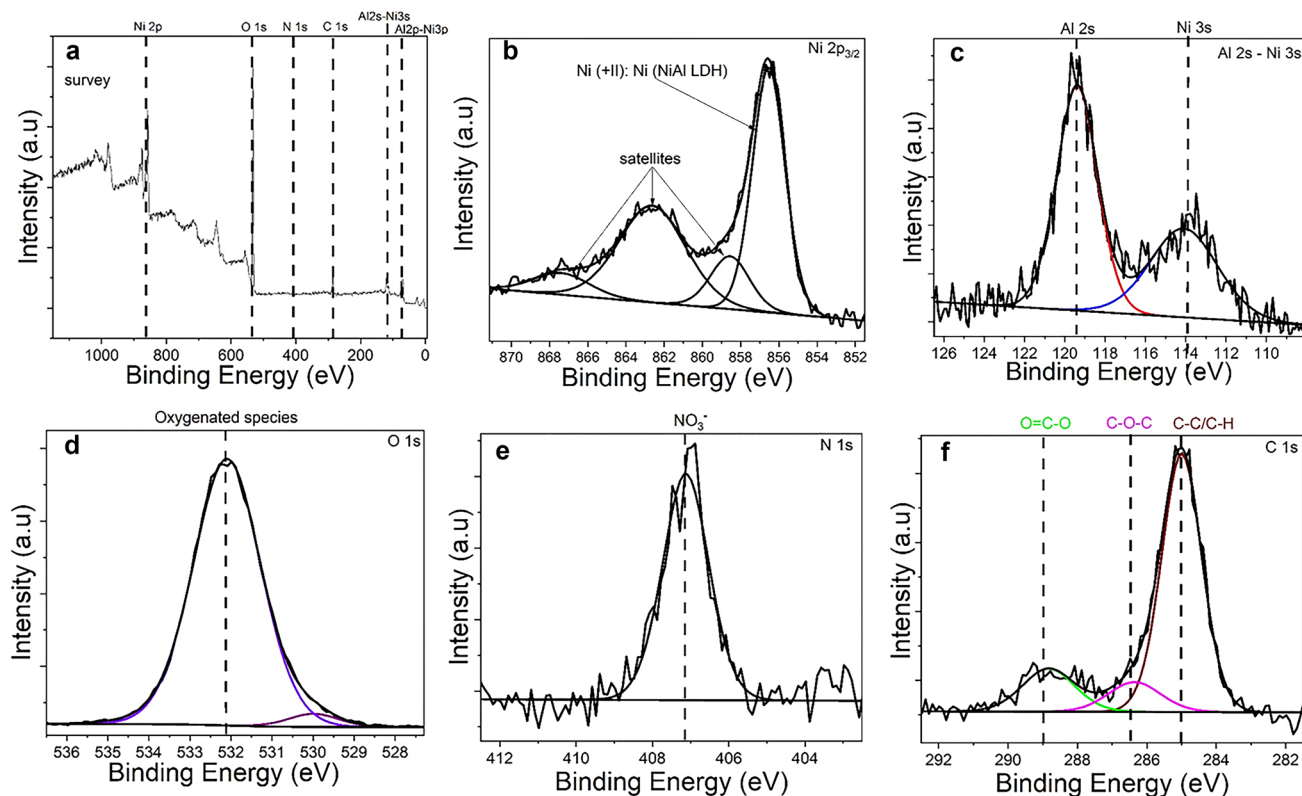


**Fig. 3** XPS spectra: **a** survey of NiAl LDH; **b** Ni  $2p_{3/2}$ ; **c** Al 2 s, **d** O 1 s; **e** N 1 s; and **f** C 1 s

broad peak located at 0.57 V is due to the reduction of the intermediate product LiOH into  $\text{Li}_2\text{O}$  and LiH [41]. The well-defined cathodic peak that appears at 0.17 V can be ascribed to the formation of the solid electrolyte interphase (SEI) films on the surface of NiAl LDH originated from the electrolyte decomposition. During the anodic sweeps, the peak at 1.03 V is due to the oxidation of LiH into LiOH [42]. The anodic peaks located at 1.48 and 2.26 V could be attributed to the decomposition of SEI, as well as the oxidation of metallic  $\text{Ni}^0$  to  $\text{Ni}^{2+}$  [43]. In addition, the presence of cathodic peaks at 0.73 V and 1.37 V after the first cycle indicates an irreversible structural or textural transformation, which occurs during the first lithiation [44]. It is worth noting that the CV sweep of the 3rd cycle can be well overlapped with that of the 2nd cycle, implying reversible electrochemical reactions in the process of lithiation/delithiation after the first cycle.

The galvanostatic charge–discharge performance of NiAl LDH electrode with SA binder at a specific current of  $50 \text{ mA g}^{-1}$  in the potential range of 0.01–3.0 V is shown in Fig. 4b. In the first lithiation curve, the long plateau at around 0.51–0.57 V is in agreement with the initial cathodic peak at approximately 0.57 V observed in the CV curve. Three sloped plateaus can be observed in the first delithiation profile, corresponding to the anodic peaks observed in

the CV curve. The NiAl LDH-SA electrode delivers 2586 and  $1578 \text{ mAh g}^{-1}$  for the first lithiation and delithiation, respectively, indicating an initial Coulombic efficiency (ICE) of 61.3%. This low ICE is due to the irreversible decomposition of the electrolyte and the formation of the SEI layer on the surface of the active material. From the second discharge profile, two discharge plateaus at around 1.49 V and 0.85 V emerge, corresponding to the cathodic peaks related to the reduction of  $\text{Ni}^{2+}$  and LiOH in the CV curves, respectively. Besides, three charge plateaus located at approximately 0.92 V, 1.46 V, and 2.22 V in the second charge profile well agree with the anodic peaks in the CV curves. Despite the capacity loss in the first cycles, a high reversible capacity of around  $1500 \text{ mAh g}^{-1}$  is achieved in the subsequent processes.

Figure 4c and d show the electrochemical features of the NiAl LDH electrode based on the PVDF binder, which is the most widely used binder in commercial electrodes for LIBs. Similar to the results shown in Fig. 4a, in Fig. 4c, the cathodic peaks at 0.5 V and 0.22 V are due to the transformation of LiOH/LiH and  $\text{Ni}^{2+}/\text{Ni}^0$ , respectively. The cathodic peak at 0.22 V also includes the electrochemical reduction of the electrolyte with the formation of the SEI film. In the anodic sweeps, the peaks centered at 1.04, 1.45, and 2.28 V are well overlapped with that of the 1st cycle and

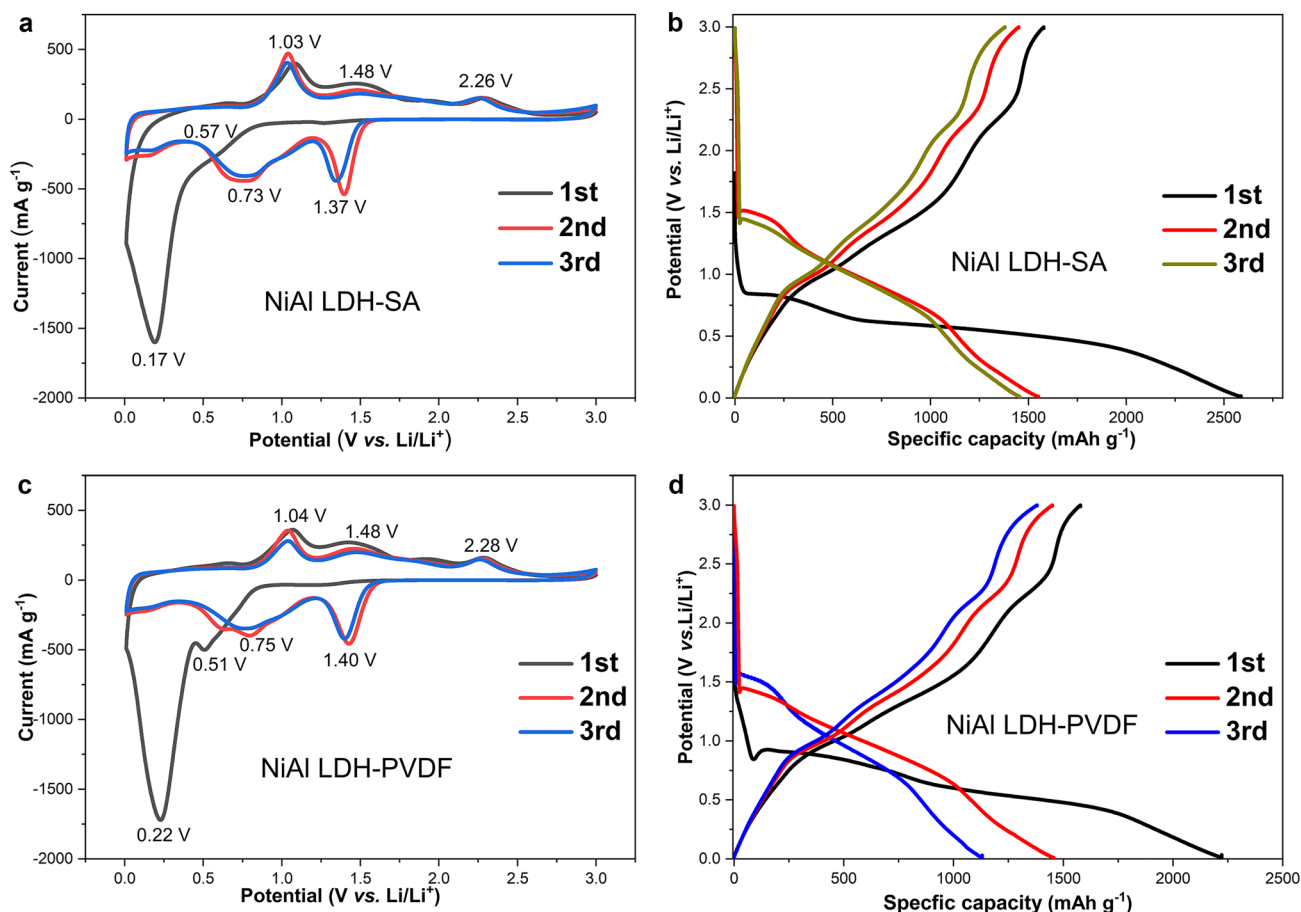


**Fig. 4** Electrochemical characterization of NiAl LDH based on different binders at the potential window of 0.01–3.0 V vs. Li/Li<sup>+</sup>. **a** CV curves at 0.1 mV s<sup>-1</sup> on the NiAl LDH-SA electrode; **b** galvanostatic charge–discharge (GCD) profiles at a current density of 0.05 A g<sup>-1</sup>

of NiAl LDH-SA electrode; **c** CV curves at 0.1 mV s<sup>-1</sup> on the NiAl LDH-PVDF electrode; **d** GCD profiles at 0.05 A g<sup>-1</sup> of the NiAl LDH-PVDF electrode

can be assigned to the reversible conversion process of LiH/LiOH and Ni<sup>0</sup>/Ni<sup>2+</sup>, respectively.

As shown in Fig. 4d, when the PVDF binder is utilized in the NiAl LDH electrode, the initial discharge and charge capacities of 2221 and 1577 mAh g<sup>-1</sup> are achieved, corresponding to an initial Coulombic efficiency of 71.0%, which is higher than what obtained with the NiAl LDH-SA electrode. During the following charge process, the decomposition of the SEI film can be responsible for the rapid capacity decay of the electrode based on both binders, as reported in the literature [45]. Although the NiAl LDH-PVDF electrode delivers comparative capacity as the NiAl LDH-SA in the first and second cycles, it presents a dramatic decay at the third cycle, suggesting inferior charge–discharge stability.

The rate capability test was performed with currents ranging from 0.05 to 10.0 A g<sup>-1</sup> and shown in Fig. 5a. The NiAl LDH-SA electrode delivers average discharge capacities of 1665, 1201, and 1051 mAh g<sup>-1</sup> at 0.05, 0.1, and 0.2 A g<sup>-1</sup>, respectively. When using PVDF as a binder, the average

discharge capacities at the same currents are 1324, 827, and 668 mAh g<sup>-1</sup>, respectively, significantly lower than those of the electrode with the SA binder. Furthermore, the NiAl LDH-SA electrode recovers to a high reversible capacity of 1109 mAh g<sup>-1</sup> when the current reverses back to 0.05 A g<sup>-1</sup>. This value is higher than the recovered capacity of 715 mAh g<sup>-1</sup> obtained with the NiAl LDH-PVDF electrode, indicating that the NiAl LDH-SA electrode is more stable and can better withstand high currents. Figure 5b depicts the cyclic performance of the two electrodes. It is worth noting that after a significant capacity decay during the first 154 cycles, the capacities of the NiAl LDH-SA electrode increase gradually. After 400 cycles, the electrode can still retain a high reversible capacity of 697 mAh g<sup>-1</sup> at the current of 0.5 A g<sup>-1</sup>. Both electrodes reach nearly 100% of Coulombic efficiency after the initial cycles, confirming the excellent reversibility of NiAl LDH and the absence of side reactions after the formation of the SEI. It is worth noting that this capacity fluctuation that appears at the 154 cycle can be influenced by

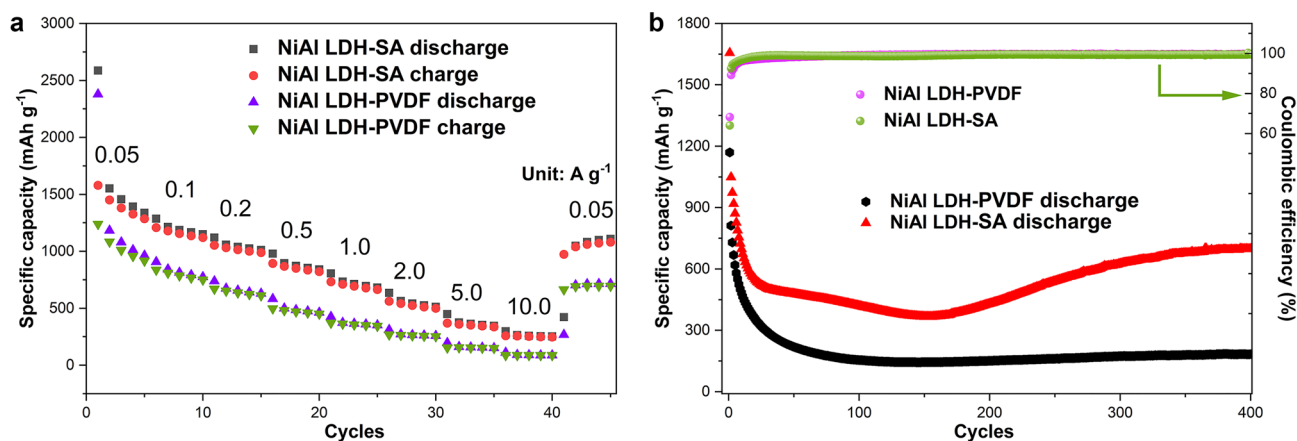


**Fig. 5** Electrochemical performance of NiAl LDH with different binders at a potential window of 0.01–3.0 V for **a** rate performance and **b** cycle performance and Coulombic efficiency at a current density of  $0.5 \text{ A g}^{-1}$

a proper selection of electrolytes such as solvent, additives, and salts as already observed in conversion materials [46].

The long-cycling performance of the NiAl LDH electrodes in the potential range of 0.01–3.0 V at the high specific current of  $1.0 \text{ A g}^{-1}$  has been further evaluated and shown in Fig. S4. A similar high initial discharge capacity ( $1405 \text{ mAh g}^{-1}$ ) is achieved by both the electrode (independently from the binder). After undergoing a capacity decay for 170 cycles, the NiAl LDH-SA electrode starts a period of capacity increase. Stable long-term cycling has been achieved with a capacity of  $388 \text{ mAh g}^{-1}$  after 1400 cycles. On the other side, the NiAl LDH-PVDF electrode shows an irreversible capacity fading after 65 cycles, with poor long-cycling performance.

To better understand the influence of binders and reactivity of NiAl LDH electrodes on the electrochemical response, we performed XPS analysis. C 1 s, F 1 s, O 1 s, and P 2p XPS spectra are presented in Fig. 6. O 1 s spectra collect signals coming from all oxygenated species present on the NiAl LDH-PVDF samples. Figure 6b and f reveals one peak centered at around 531.5 eV, which is characteristic of the mix of O=C and  $\text{Li}_2\text{CO}_3$  components in the battery system with DMC as the solvent. Three additional elements center at 530.3 eV (the combination of ROLi/LiOH), 533.6 eV (O–C and P–O environments), and 528.5 eV (attributed to  $\text{O}^{2-}$  anions from  $\text{Li}_2\text{O}$  component) are presented in the spectra, respectively. Another peak that appears at 537.8 eV is assigned to Na KLL from sodium present in the SA binder, which is always present in O 1 s spectra of sodium-based samples.

Figure 6c and g show the spectra of F 1 s, one component located at 685.0 eV confirming the presence of LiF (on all cycled electrode samples), and the other situated at around 687.1 eV indicating the presence of P–F component from  $\text{LiPF}_6$  and  $\text{CF}_2\text{--CH}_2$  component from PVDF

(only present on NiAl LDH-PVDF samples). Besides, P 2p spectra (Fig. 6d and h) have to be fitted with  $2p_{3/2}\text{--}2p_{1/2}$  doublets separated by 0.9 eV with a 2/1 intensity ratio due to spin–orbit coupling. The main doublet with P  $2p_{3/2}$  component located at 133.6 eV is the phosphates signal from the decomposition of  $\text{LiPF}_6$ , and the other at around 137 eV corresponds to the phosphorus from  $\text{LiPF}_6$ .

The C 1 s spectra (Fig. 6a and e) comprise one component (located at 283.3 eV) characteristic of the carbon black (CB). The three components at 286.2 eV (attributed to the  $\text{CH}_2$  chemical environment in PVDF binder), 290.7 eV ( $\text{CF}_2\text{--CH}_2$ ), and 291.8 eV ( $\text{CF}_2\text{--CF}_2$ ) confirm the presence of the PVDF binder on the surface of the electrode [47]. The four other components at 285 eV (C–C/C–H), 286.8 eV (mix of C–O/ROLi) [48], 288.5 eV (C=O), and 290.1 eV (attributed to the  $\text{Li}_2\text{CO}_3$  chemical environment) are due to the degradation products of the electrolyte which are composing the SEI. These components remain on the electrodes during electrochemical measurements. For the NiAl LDH-PVDF electrode, the intensity of the components attributed to CB slightly increases after discharging to 0.22 V, indicating the thinning down of the SEI film. While for the NiAl LDH-SA electrode, the CB components decrease, suggesting a thicker up of the SEI. The change of C 1 s spectra after the full cycle reveals a thicker SEI formation on the NiAl LDH-SA electrode. This difference may be due to the gelation derived from a stronger interaction of PVDF binder and electrolyte, which hinders the further formation of SEI film [49].

XPS analysis of NiAl LDH after cycling confirms a similar SEI composition for the electrode with both binders. The species of  $\text{Li}_2\text{O}$  (from NiAl LDH-SA samples), LiF, a mix of ROLi/LiOH,  $\text{Li}_2\text{CO}_3$ , and phosphates, which are decomposition products of electrolyte during cycling, are detected with XPS on all samples. Furthermore, compared with the NiAl LDH-PVDF electrode, a less amount



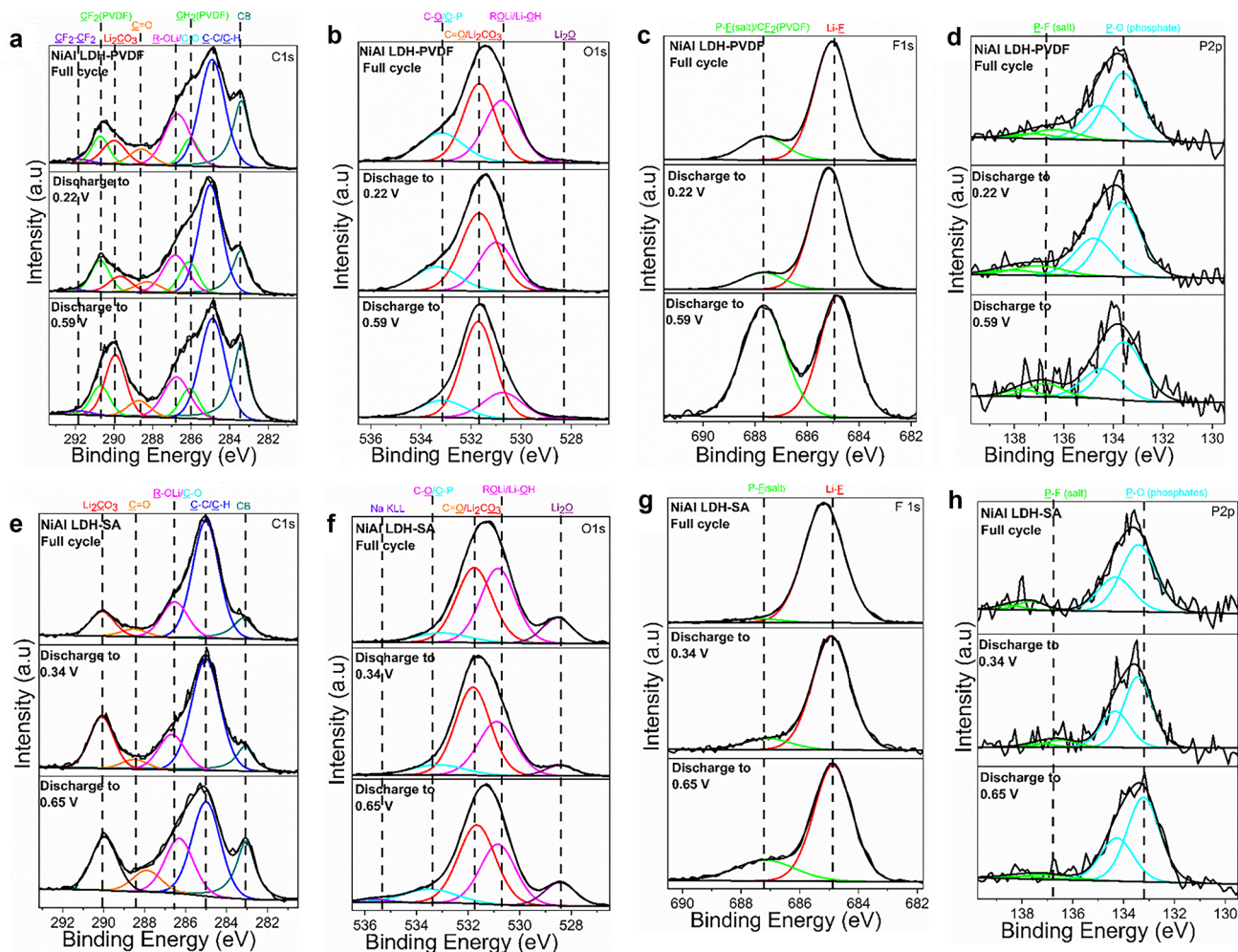


**Fig. 6** **a** C 1s, **b** O 1s, **c** F 1s, and **d** P 2p XPS spectra of NiAl LDH-PVDF electrode discharged to 0.59 V and 0.22 V and charged to 3.0 V (1 cycle) respectively; **e** C 1s, **f** O 1s, **g** F 1s, and **h** P

2p XPS spectra of NiAl LDH-SA electrode discharged to 0.65 V and 0.34 V and charged to 3.0 V (1 cycle), respectively

of LiF and a higher amount of Oxygen (from oxidized species) on the NiAl LDH-SA electrode surface are found, which suggests a higher electrolyte degradation when SA is used as the binder. Fig. S5 shows the binder's influence on the concentration of the species that make up the SEI film. The use of PVDF as a binder on the electrode can promote the LiF formation, which is found in less amount on the NiAl LDH-SA electrode. In comparison, the SA binder facilitates lithium oxide formation such as  $\text{Li}_2\text{O}$ , ROLi, and LiOH. Moreover, the quantity of these species remains stable during the first full cycle. The lower solubility of lithium oxide with respect to LiF in carbonate electrolytes brings about a stable SEI film [50]. As a result, the stable lithium oxide component in SEI film could be a dominant source of anode passivation. The thicker and stable SEI film detected when using SA as binder might be the reason for the higher irreversible capacity at the first

cycle and for the better cycling stability as compared to the PVDF-based electrode.

According to recent reports [51–54], the potential discharge cutoff can influence the cycling stability. Indeed, a higher potential discharge cutoff can prevent the complete reduction of  $\text{Ni}^{2+}$  to  $\text{Ni}^0$  and can result in a different SEI. Figure 7 and Fig. S6 report the CV and GCPL curves recorded on the two electrodes in the potential range 0.4–3.0 vs. Li<sup>+</sup>/Li. The NiAl LDH-SA and NiAl LDH-PVDF electrodes show similar CV shapes during the first cycle (black curves in Fig. 7a and c). A weak peak at 1.23 V can be observed during lithiation, which is attributed to the reduction of  $\text{Ni}^{2+}$  to  $\text{Ni}^+$  and the simultaneous intercalation of  $\text{Li}^+$ . This peak strengthens during the following cycles, suggesting the domination of the  $\text{Ni}^+/\text{Ni}^{2+}$  transformation. A distinct cathodic peak appears when discharging to 0.6 V, suggesting the reduction of the



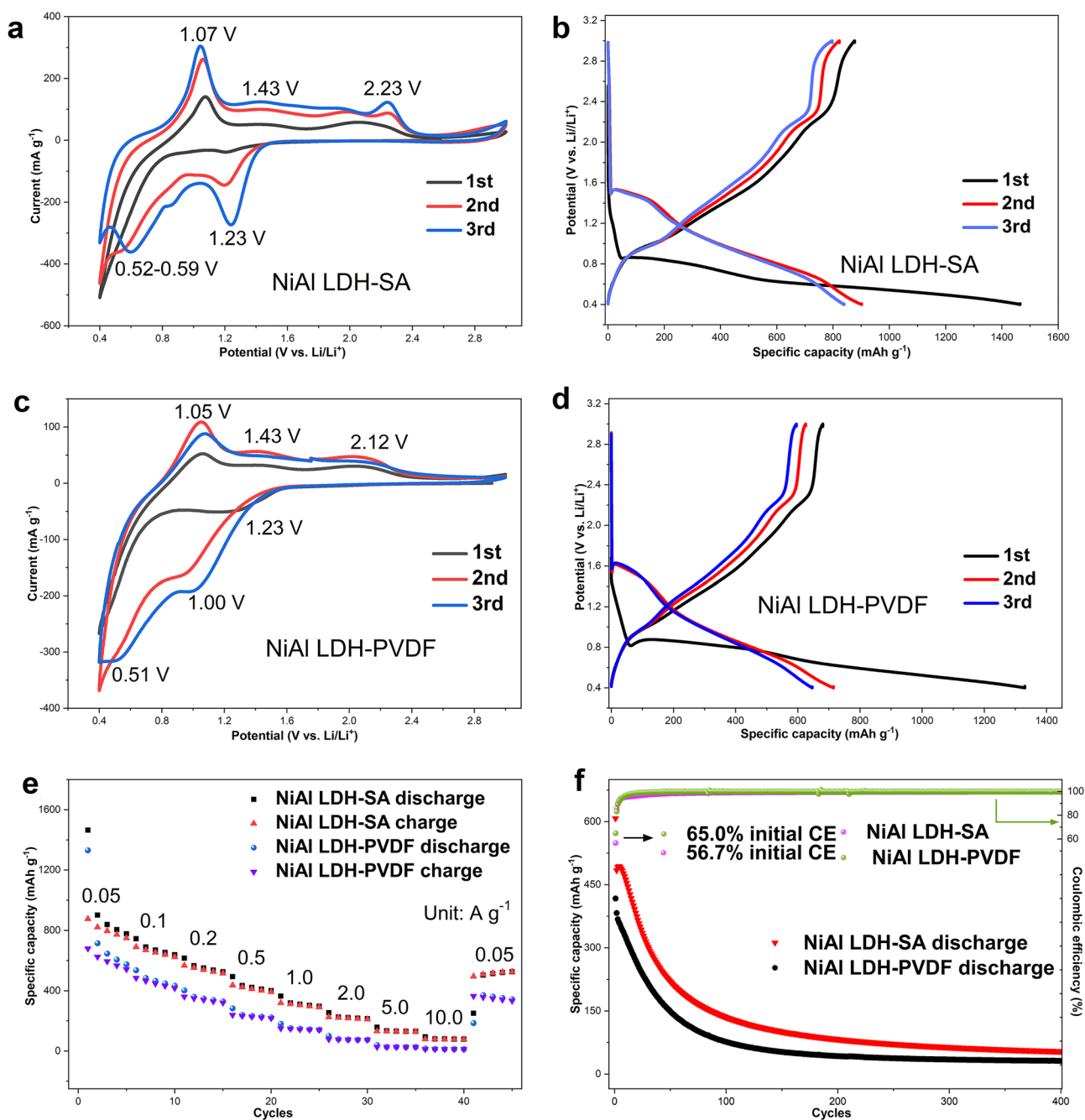


**Fig. 7** Electrochemical performance of NiAl LDH with different binders in the potential range of 0.4–3.0 V. **a** CV curves at a scan rate of  $0.1 \text{ mV s}^{-1}$  for NiAl LDH-SA electrode; **b** GCD curves at a current density of  $0.05 \text{ A g}^{-1}$  for NiAl LDH-SA electrode; **c** CV curves at a scan rate of  $0.1 \text{ mV s}^{-1}$  for NiAl LDH-PVDF electrode; **d** GCD

curves at a current density of  $0.05 \text{ A g}^{-1}$  for NiAl LDH-PVDF electrode; **e** rate capacity at different current densities of SA and PVDF-based electrodes; and **f** cycle performance and Coulombic efficiency at a current density of  $0.5 \text{ A g}^{-1}$  of NiAl LDH-SA and NiAl LDH-PVDF electrodes

intermediate product LiOH into  $\text{Li}_2\text{O}$  and LiH as well as the formation of the SEI films. The anodic peak at 1.07 V accounts for the oxidation of  $\text{Li}_2\text{O}$  into LiOH [42], and the other anodic peak at around 2.23 V can be correlated to the conversion of Ni into nickel hydroxide.

The weak anodic peak appearing at 1.43 V may be attributed to the decomposition of SEI film [55, 56]. The reduction peak at around 1.23 V of the NiAl LDH-SA electrode shows almost no shift in the following cycles (Fig. 7a). In comparison, the corresponding reduction peak of the NiAl

LDH-PVDF electrode (Fig. 7c), with cycling, shifts to more negative potentials, from 1.23 V to around 1.00 V, indicating an increase in electrode polarization [57, 58].

The GCD performance of the NiAl LDH electrode based on SA and PVDF binders at 0.4–3.0 V was further investigated (Fig. 7b and d). The initial discharge capacity of the NiAl LDH-SA electrode is 1465 mAh g<sup>-1</sup>, which is higher than that of the NiAl LDH-PVDF electrode (1330 mAh g<sup>-1</sup>). The corresponding initial Coulombic efficiencies are 60.0% and 51.1%, respectively. Besides, the SA binder-based electrode shows more well-defined lithiation and delithiation plateaus in the subsequent sweep profiles.

Figure 7e shows the rate test of the NiAl LDH electrode with the two different binders at current densities from 0.05–10.0 A g<sup>-1</sup>. The average discharge capacities of the NiAl LDH-SA electrode are 957, 679, and 559 mAh g<sup>-1</sup> at 0.05, 0.1, and 0.2 A g<sup>-1</sup>, respectively, and a reversible capacity of 526 mAh g<sup>-1</sup> is recovered when the current rate returns to 0.05 A g<sup>-1</sup> after 45 cycles, corresponding to a 58% of retention at 0.2 A g<sup>-1</sup>. As a comparison, the NiAl LDH-PVDF electrode provides an average capacity of 774, 474, and 356 mAh g<sup>-1</sup> at 0.05, 0.1, and 0.2 A g<sup>-1</sup>, respectively, along with a lower restored capacity at 0.05 A g<sup>-1</sup> after 45 cycles (343 mAh g<sup>-1</sup>) and lower retention at 0.2 A g<sup>-1</sup> (46%).

Figure 7f shows the long-term cycling experiment on the two electrodes in the restricted potential range at 0.5 A g<sup>-1</sup>. The NiAl LDH-SA electrode delivers a higher initial discharge capacity (607 mAh g<sup>-1</sup>) and Coulombic efficiency (65.0%) than the NiAl LDH-PVDF electrode (417 mAh g<sup>-1</sup> and 56.7%, respectively). However, in the potential window 0.4–3.0 V, in contrast to what was obtained in the extended potential region of 0.01–3.0 V, both electrodes suffer from poor cycling retention (< 10% after 400 cycles). These results demonstrate that the small cutoff potential of the NiAl LDH electrode can dramatically affect the delivered capacity and the cycling stability. This finding is the

opposite of what was observed with another LDH composite electrode (CoFe LDH with nitrates in the interlayer) tested in 1 M NaCF<sub>3</sub>SO<sub>3</sub>/Diglyme on sodium-ion batteries, where the electrode at a potential window of 0.4–3.0 V vs. Na<sup>+</sup>/Na resulted in improved stability compared with the CoFe LDH electrode in a smaller cutoff potential (0.01 V vs. Na<sup>+</sup>/Na) at 1 A g<sup>-1</sup> after 200 cycles [52].

Furthermore, CV at different scan rates of NiAl LDH electrodes at 0.4–3.0 V was performed (Fig. S7) to better understand the electrochemical reaction kinetics. With increasing the scan rate, the CV shape is retained and the peak positions (Fig. S7a and b) gradually change, which suggests low resistance and mild polarization [59]. Bulk ion diffusion controlled and capacitive effect behaviors can be revealed from the equation describing the relationship of peak current (*i*) and scan rate (*v*) [60, 61]:

$$i = av^b$$

A *b* value of ~0.5 indicates a diffusion-controlled process, while a value ~1 indicates a capacitive surface-controlled effect. The parameter *b* can be expressed as the slope of the log(*v*)-log(*i*) plot. Regarding the SA binder-based electrode, the *b*-values of anodic peak 1 and peak 2 are 0.92 and 0.90, respectively (Fig. S7c). The *b*-values of the anodic peak 1 (0.84) and peak 2 (0.85) of the PVDF binder-based electrode are consistent with that of the SA-based electrode, revealing that the intercalation of Li-ion within the NiAl LDH electrode is a surface-dominated process, independently from the binder.

To understand the redox processes occurring on the NiAl LDH electrode during the 1st cycle, XAS measurements were performed on ex situ samples. Normalized Ni K-edge XANES spectra and Fourier transform (FT) of the recorded EXAFS spectra are displayed in Fig. 8. The ex situ samples consist of lithiated (0.4 V, 0.01 V) and delithiated (3.0 V after 0.4 V, 3.0 V after 0.01 V) NiAl LDH electrodes. The current used to bring the electrodes to the desired potential is

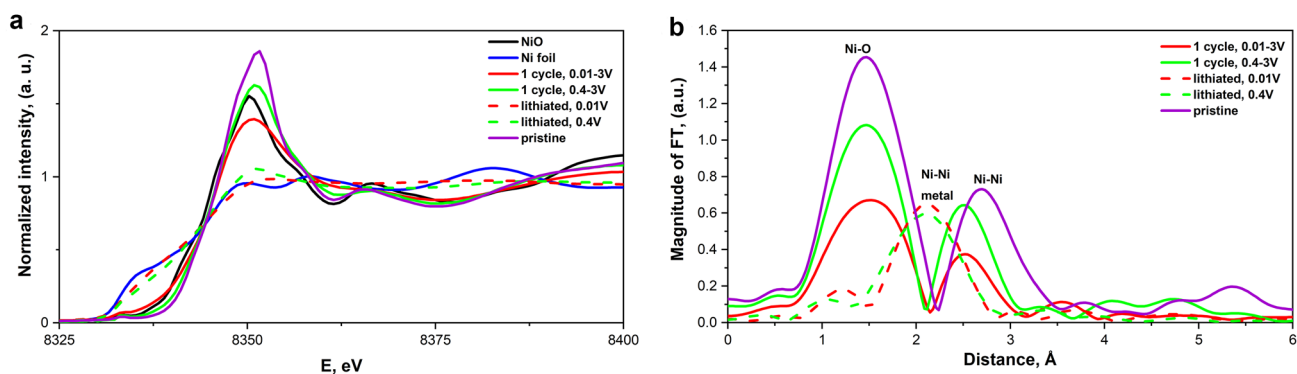
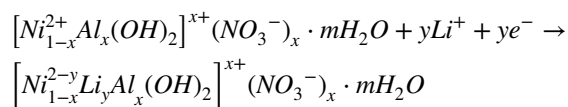


**Fig. 8** **a** Normalized XANES spectra at Ni K-edge and, **b** Fourier transform of the recorded EXAFS spectra collected on ex situ samples

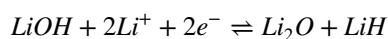
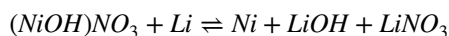
0.05 A g<sup>-1</sup>. The Ni K-edge (Fig. 8a) of the NiAl LDH shifts to lower energies after lithiation to 0.01 V, confirming the conversion reaction Ni<sup>2+</sup> → Ni<sup>0</sup> at this potential. According to FT EXAFS spectra, the pristine NiAl LDH shows two distinct peaks at around 1.4 and 2.7 Å, corresponding to the 1st and 2nd Ni coordination shells in the initial structure, accordingly. The Ni metal phase is obtained when the peak corresponding to the Ni–Ni band in the metal structure appears at around 2.1 Å on the FT EXAFS spectra (sample lithiated to 0.4 V). In agreement with the ex situ XRD data, this result shows that the appearance of the Ni metallic fraction is accompanied by the amorphization of the initial NiAl LDH structure (Fig. S8). Based on the ex situ XAS and XPS measurements, by stopping the electrochemical reduction to 0.4 V, the SEI is not completely formed and the conversion reaction is only started but not completed. This can reflect the worst stability of the electrodes cycled at the cutoff potential of 0.4 V. On the other side, when the sample is discharged to the lowest potential of 0.01 V, the diffraction reflections of another product of the conversion reaction of LiOH can be recognized. Besides, the pristine NiAl LDH material does not return to the initial oxidation state after one cycle and the Ni remains slightly reduced, explaining the fast capacity loss of NiAl LDH. The mechanism of the electrochemical reaction occurring during the first cycle can be proposed as two steps process:

- 1) Intercalation (corresponding to the potential range of 3.0 V–0.5 V)



$$(1 < y \leq 2)$$

- 2) Conversion (corresponding to the long plateau at around 0.5 V)



## Conclusion

In summary, NiAl LDH material with NO<sub>3</sub><sup>-</sup> as the interlayer anion was applied as a negative electrode on lithium-ion batteries and the role of the binder (PVDF and SA) and of the potential cutoff was evaluated. The NiAl LDH electrode with SA binder shows a high capacity and more

stable cycling ability than the electrode with PVDF binder. A higher amount of lithium oxide component at the surface of the NiAl LDH-SA electrode is detected by XPS. Since Li<sub>2</sub>O is less soluble in carbonate-based solvents than the LiF (detected as a major SEI component in the PDVF-based electrode), the resulting SEI should be more stable and explains the better cycling ability of the SA-based electrode. Furthermore, the NiAl LDH electrode at the discharge cutoff potential of 0.01 V can achieve a longer cycling life in comparison to the electrode at a discharge cutoff potential of 0.4 V owing to a complete conversion reaction and a complete SEI formation in the potential range of 0.01–3.0 V (vs. Li/Li<sup>+</sup>). Ex situ XAS confirms that the NiAl LDH stores Li<sup>+</sup> via a conversion mechanism (Ni<sup>2+</sup> to Ni<sup>0</sup>) in the potential range of 0.01–3.0 V (vs. Li/Li<sup>+</sup>). Hence, this work clearly shows that the environmentally friendly sodium alginate binder, applied to NiAl LDH, improves the electrochemical performance of this material in LIBs. Future studies should focus on addressing the irreversible capacity loss issue that is an overall problem for LDH materials; overcoming such a problem can open up a broad possibility of applying LDH materials on ion storage batteries.

**Supplementary Information** The online version contains supplementary material available at <https://doi.org/10.1007/s10008-021-05011-y>.

**Acknowledgements** This work contributes to the research performed at CELEST (Center for Electrochemical Energy Storage Ulm-Karlsruhe). The authors thank Prof. Helmut Ehrenberg for his support on this work and the fruitful discussions. The authors acknowledge the beamline scientists Edmund Welter and Morgane Desmau from beamline P65, DESY (Hamburg, Germany), to provide the experimental facilities and give instructions.

**Funding** Open Access funding enabled and organized by Projekt DEAL. X.L. received financial support from the China Scholarship Council (CSC No. 201807565019, [2018] 3101) to pursue her Ph.D. degree at KIT (Karlsruhe Institute of Technology).

**Data availability** The data that support the findings of this study are available under DOI: [10.5445/IR/1000135718](https://doi.org/10.5445/IR/1000135718) and from the corresponding author upon request.

**Open Access** This article is licensed under a Creative Commons Attribution 4.0 International License, which permits use, sharing, adaptation, distribution and reproduction in any medium or format, as long as you give appropriate credit to the original author(s) and the source, provide a link to the Creative Commons licence, and indicate if changes were made. The images or other third party material in this article are included in the article's Creative Commons licence, unless indicated otherwise in a credit line to the material. If material is not included in the article's Creative Commons licence and your intended use is not permitted by statutory regulation or exceeds the permitted use, you will need to obtain permission directly from the copyright holder. To view a copy of this licence, visit <http://creativecommons.org/licenses/by/4.0/>.

## References

- Mahmood N, Tang T, Hou Y (2016) Nanostructured anode materials for lithium ion batteries: progress, challenge and perspective. *Adv Energy Mater* 6:1–22
- Lu J, Chen Z, Pan F et al (2018) High-performance anode materials for rechargeable lithium-ion batteries. *Electrochem Energy Rev* 1:35–53
- Chu S, Majumdar A (2012) Opportunities and challenges for a sustainable energy future. *Nature* 488:294–303
- Bandhauer TM, Garimella S, Fuller TF (2011) A critical review of thermal issues in lithium-ion batteries. *J Electrochem Soc* 158:R1
- Armand M, Tarascon JM (2008) Building better batteries. *Nature* 451:652–657
- Li B, Cao H, Shao J et al (2011) Improved performances of  $\beta$ -Ni(OH)<sub>2</sub>@reduced-graphene-oxide in Ni-MH and Li-ion batteries. *Chem Commun* 47:3159–3161
- Liu Z, Tay SW, Li X (2011) Rechargeable battery using a novel iron oxide nanorods anode and a nickel hydroxide cathode in an aqueous electrolyte. *Chem Commun* 47:12473–12475
- Hu YY, Liu Z, Nam KW et al (2013) Origin of additional capacities in metal oxide lithium-ion battery electrodes. *Nat Mater* 12:1130–1136
- Wang C, Zhang X, Xu Z et al (2015) Ethylene glycol intercalated cobalt/nickel layered double hydroxide nanosheet assemblies with ultrahigh specific capacitance: structural design and green synthesis for advanced electrochemical storage. *ACS Appl Mater Interfaces* 7:19601–19610
- Cavani F, Trifirò F, Vaccari A (1991) Hydrotalcite-type anionic clays: preparation, properties and applications. *Catal Today* 11:173–301
- Goh KH, Lim TT, Dong Z (2008) Application of layered double hydroxides for removal of oxyanions: a review. *Water Res* 42:1343–1368
- Song F, Hu X (2014) Exfoliation of layered double hydroxides for enhanced oxygen evolution catalysis. *Nat Commun* 5
- Feng J, He Y, Liu Y et al (2015) Supported catalysts based on layered double hydroxides for catalytic oxidation and hydrogenation: general functionality and promising application prospects. *Chem Soc Rev* 44:5291–5319
- Fan G, Li F, Evans DG, Duan X (2014) Catalytic applications of layered double hydroxides: recent advances and perspectives. *Chem Soc Rev* 43:7040–7066
- Mishra G, Dash B, Pandey S (2018) Layered double hydroxides: a brief review from fundamentals to application as evolving biomaterials. *Appl Clay Sci* 153:172–186
- Mishra G, Dash B, Sethi D et al (2017) Orientation of organic anions in Zn-Al layered double hydroxides with enhanced antibacterial property. *Environ Eng Sci* 34:516–527
- Zubair M, Daud M, McKay G et al (2017) Recent progress in layered double hydroxides (LDH)-containing hybrids as adsorbents for water remediation. *Appl Clay Sci* 143:279–292
- Patel R, Park JT, Patel M et al (2017) Transition-metal-based layered double hydroxides tailored for energy conversion and storage. *J Mater Chem A* 6:12–29
- Chen J, Li S, Qian K, Lee PS (2018) NiMn layered double hydroxides derived multiphase Mn-doped Ni sulfides with reduced graphene oxide composites as anode materials with superior cycling stability for sodium ion batteries. *Mater Today Energy* 9:74–82
- Lai F, Miao YE, Zuo L et al (2016) Biomass-derived nitrogen-doped carbon nanofiber network: a facile template for decoration of ultrathin nickel-cobalt layered double hydroxide nanosheets as high-performance asymmetric supercapacitor electrode. *Small* 12:3235–3244
- Li X, Yu L, Wang G et al (2017) Hierarchical NiAl LDH nanotubes constructed via atomic layer deposition assisted method for high performance supercapacitors. *Electrochim Acta* 255:15–22
- Li X, Wan G, Xiao J et al (2018) Carbon-coated Ni(OH)<sub>2</sub>-NiAl LDH hierarchical nanostructures on Ni foam as a high areal capacitance electrode for supercapacitor application. *Mater Lett* 228:179–182
- Shi L, Chen Y, He R et al (2018) Graphene-wrapped CoNi-layered double hydroxide microspheres as a new anode material for lithium-ion batteries. *Phys Chem Chem Phys* 20:16437–16443
- Zhang S, Zhang L, Xu G-C, et al (2020) PVP-assisted construction of Co<sub>3</sub>V<sub>2</sub>O<sub>8</sub>@NiCo LDH hierarchical structure for high-performance lithium-ion batteries. *New J Chem* 0–5
- Li W, Lee S, Manthiram A (2020) High-nickel NMA: a cobalt-free alternative to NMC and NCA cathodes for lithium-ion batteries. *Adv Mater* 32:1–6
- Yan P, Zheng J, Liu J et al (2018) Tailoring grain boundary structures and chemistry of Ni-rich layered cathodes for enhanced cycle stability of lithium-ion batteries. *Nat Energy* 3:600–605
- Li BM, Lu J (2020) Cobalt in lithium-ion batteries. *Science* 367:979–980
- Zhang M, Wei Z, Wang T et al (2019) Nickel-iron layered double hydroxides and reduced graphene oxide composite with robust lithium ion adsorption ability for high-capacity energy storage systems. *Electrochim Acta* 296:190–197
- Wang R, Feng L, Yang W et al (2017) Effect of different binders on the electrochemical performance of metal oxide anode for lithium-ion batteries. *Nanoscale Res Lett* 12:575
- Liu H, Yu T, Su D et al (2017) Ultrathin Ni-Al layered double hydroxide nanosheets with enhanced supercapacitor performance. *Ceram Int* 43:14395–14400
- Roisnel T, Rodriguez-Carvajal J (2001) WinPLOTR: a windows tool for powder diffraction pattern analysis. *Mater Sci Forum* 378–381:118–123
- Scofield JH (1976) Hartree-Slater subshell photoionization cross-sections at 1254 and 1487 eV. *J Electron Spectroscop Relat Phenomena* 8:129–137
- Tyagi A, Myung Y, Tripathi KM, et al (2020) High-performance hybrid microsupercapacitors based on Co–Mn layered double hydroxide nanosheets. *Electrochim Acta* 334:135590
- Shabanian M, Hajibeygi M, Raeisi A (2020) FTIR characterization of layered double hydroxides and modified layered double hydroxides. Elsevier Ltd
- Lim SY, Lee JH, Kim S et al (2017) Lattice water for the enhanced performance of amorphous iron phosphate in sodium-ion batteries. *ACS Energy Lett* 2:998–1004
- Sai Gautam G, Canepa P, Richards WD et al (2016) Role of structural H<sub>2</sub>O in intercalation electrodes: the case of Mg in nanocrystalline xerogel-V<sub>2</sub>O<sub>5</sub>. *Nano Lett* 16:2426–2431
- Roberts MW, Smart RSC (1984) The defect structure of nickel oxide surfaces as revealed by photoelectron spectroscopy. *J Chem Soc Faraday Trans 1 Phys Chem Condens Phases* 80:2957–2968
- Moroney LM, Smart RSC, Roberts MW (1983) Studies of the thermal decomposition of  $\beta$ -NiO(OH) and nickel peroxide by X-ray photoelectron spectroscopy. *J Chem Soc Faraday Trans 1 Phys Chem Condens Phases* 79:1769–1778
- Liu S, Lee SC, Patil U et al (2017) Hierarchical MnCo-layered double hydroxides@Ni(OH)<sub>2</sub> core-shell heterostructures as advanced electrodes for supercapacitors. *J Mater Chem A* 5:1043–1049
- Greczynski G, Hultman L (2020) Compromising science by ignorant instrument calibration—need to revisit half a century of published XPS data. *Angew Chemie* 132:5034–5038
- Zhang R, Xue Z, Qin J et al (2020) NiCo-LDH/Ti<sub>3</sub>C<sub>2</sub> MXene hybrid materials for lithium ion battery with high-rate capability and long cycle life. *J Energy Chem* 50:143–153



42. Yao J, Li Y, Huang R et al (2021) Crucial role of water content on the electrochemical performance of  $\alpha$ -Ni(OH)<sub>2</sub> as an anode material for lithium-ion batteries. *Ionics (Kiel)* 27:65–74
43. Zhai Z, Liu Q, Zhu Y et al (2019) Synthesis of Ni(OH)<sub>2</sub>/graphene composite with enhanced electrochemical property by stirring solvothermal method. *J Alloys Compd* 775:1316–1323
44. Bai Z, Ju Z, Guo C et al (2014) Direct large-scale synthesis of 3D hierarchical mesoporous NiO microspheres as high-performance anode materials for lithium ion batteries. *Nanoscale* 6:3268–3273
45. Kabir M, Demirocak D (2017) Degradation mechanisms in Li-ion batteries: a state-of -the-art review. *Int J Energy Res* 41:1963–1986
46. Zhao Z, Gehrlein L, Bothe A, et al (2021) Impact of 3-cyanopropionic acid methyl ester on the electrochemical performance of ZnMn<sub>2</sub>O<sub>4</sub> as negative electrode for Li-ion batteries . *Energy Technol* 2100247
47. Gieu JB, Courrèges C, El Ouatani L et al (2016) Temperature effects on Li<sub>4</sub>Ti<sub>5</sub>O<sub>12</sub> electrode/electrolyte interfaces at the first cycle: a X-ray photoelectron spectroscopy and scanning Auger microscopy study. *J Power Sources* 318:291–301
48. Leroy S, Blanchard F, Dedryvère R et al (2005) Surface film formation on a graphite electrode in Li-ion batteries: AFM and XPS study. *Surf Interface Anal* 37:773–781
49. Buqa H, Holzapfel M, Krumeich F et al (2006) Study of styrene butadiene rubber and sodium methyl cellulose as binder for negative electrodes in lithium-ion batteries. *J Power Sources* 161:617–622
50. Tasaki K, Goldberg A, Lian J-J et al (2009) Solubility of lithium salts formed on the lithium-ion battery negative electrode surface in organic solvents. *J Electrochem Soc* 156:A1019
51. Zhang X, Liu K, Zhang S, et al (2020) Enabling remarkable cycling performance of high-loading MoS<sub>2</sub>@Graphene anode for sodium ion batteries with tunable cut-off voltage. *J Power Sources* 458:228040
52. Zhao Y, Sun T, Yin Q et al (2019) Discovery of a new intercalation-type anode for high-performance sodium ion batteries. *J Mater Chem A* 7:15371–15377
53. Rahman MM, Rani RA, Sadek AZ et al (2013) A vein-like nanoporous network of Nb<sub>2</sub>O<sub>5</sub> with a higher lithium intercalation discharge cut-off voltage. *J Mater Chem A* 1:11019–11025
54. Ding Y, Yang Y, Shao H (2011) High capacity ZnFe<sub>2</sub>O<sub>4</sub> anode material for lithium ion batteries. *Electrochim Acta* 56:9433–9438
55. Ni S, Lv X, Li T et al (2013) The investigation of Ni(OH)<sub>2</sub>/Ni as anodes for high performance Li-ion batteries. *J Mater Chem A* 1:1544–1547
56. Zhu X, Zhong Y, Zhai H et al (2014) Nanoflake nickel hydroxide and reduced graphene oxide composite as anode materials for high capacity lithium ion batteries. *Electrochim Acta* 132:364–369
57. Zhang S, Ren S, Han D et al (2019) Aqueous sodium alginate as binder: dramatically improving the performance of dilithium terephthalate-based organic lithium ion batteries. *J Power Sources* 438:22700717
58. Zhou J, Li J, Liu K et al (2014) Free-standing cobalt hydroxide nanoplatelet array formed by growth of preferential-orientation on graphene nanosheets as anode material for lithium-ion batteries. *J Mater Chem A* 2:20706–20713
59. Luo XF, Yang CH, Peng YY et al (2015) Graphene nanosheets, carbon nanotubes, graphite, and activated carbon as anode materials for sodium-ion batteries. *J Mater Chem A* 3:10320–10326
60. Brezesinski T, Wang J, Tolbert SH, Dunn B (2010) Ordered mesoporous  $\alpha$ -MoO<sub>3</sub> with iso-oriented nanocrystalline walls for thin-film pseudocapacitors. *Nat Mater* 9:146–151
61. Chao D, Zhu C, Yang P et al (2016) Array of nanosheets render ultrafast and high-capacity Na-ion storage by tunable pseudocapacitance. *Nat Commun* 7:1–8

**Publisher's Note** Springer Nature remains neutral with regard to jurisdictional claims in published maps and institutional affiliations.